

DRAFT VERSION DECEMBER 22, 2025
 Typeset using **L^AT_EX preprint2** style in AASTeX631

Asymptotic behaviour of galactic small-scale dynamos at modest magnetic Prandtl number

FREDERICK A. GENT,^{1,2,3} MORDECAI-MARK MAC LOW,⁴ MAARIT J. KORPI-LAGG,^{2,1} TOUKO PURO,²
 AND MATTHIAS REINHARDT²

¹*Nordita, KTH Royal Institute of Technology and Stockholm University, Hannes Alfvéns väg 12, Stockholm, SE-106 91 Stockholm, Sweden*

² *HPCLab, Department of Computer Science, Aalto University, P.O. Box 15400, FI-00076 Espoo, Finland*

³ *School of Mathematics, Statistics and Physics, Newcastle University, NE1 7RU, UK*

⁴ *Department of Astrophysics, American Museum of Natural History, New York, NY 10024, USA*

(Received December 22, 2025; Revised December 22, 2025; Accepted)

Submitted to ApJL

ABSTRACT

Magnetic fields are critical at many scales to galactic dynamics and structure, including multiphase pressure balance, dust processing, and star formation. Dynamo action determines their dynamical structure and strength. Simulations of combined large- and small-scale dynamos have successfully developed mean fields with strength and topology consistent with observations but with turbulent fields much weaker than observed, while simulations of small-scale dynamos with parameters relevant to the interstellar medium yield turbulent fields an order of magnitude below the values observed or expected theoretically. We use the PENCIL CODE accelerated on GPUs with ASTAROTH to perform high-resolution simulations of a supernova-driven galactic dynamo including heating and cooling in a periodic domain. Our models show that the strength of the turbulent field produced by the small-scale dynamo approaches an asymptote at only modest magnetic Prandtl numbers. This allows us to use these models to suggest the essential characteristics of this constituent of the magnetic field for inclusion in global galactic models. The asymptotic limit occurs already at magnetic Prandtl number of only a few hundred, many orders of magnitude below physical values in the the interstellar medium and consistent with previous findings for isothermal compressible flows.

Keywords: dynamo — magnetohydrodynamics (MHD) — ISM: supernova remnants — ISM: magnetic fields — turbulence

Corresponding author: Frederick A. Gent
 Email: frederick.gent@su.se, mordecai@amnh.org,
maarit.korpi-lagg@aalto.fi, touko.puro@aalto.fi,
matthias.rheinhardt@aalto.fi

1. INTRODUCTION

We report on the results of unprecedentedly high-resolution simulations of supernova (SN)-

driven turbulence in the interstellar medium (ISM) using the GPU-accelerated PENCIL CODE on the exascale resources of the LUMI supercomputer¹. We reach higher magnetic Reynolds numbers than previously possible in the modelling of the *small-scale dynamo* (SSD) in the ISM. These results improve our understanding of how the turbulent magnetic field may be included more generally in simulations of galaxy formation and evolution.

Modelling the growth of galactic magnetic fields requires resolving the large separation between driving and turbulent diffusion scales. Simulations of large-scale dynamos (LSDs) have yielded solutions with large-scale fields matching the topology and field strength of those observed but with a turbulent constituents an order of magnitude weaker (Gressel 2008; Gent 2012; Gent et al. 2024). In contrast, observations determine the turbulent field constituent to be as much as ten times stronger than the mean field (Beck 2015; Beck & Berkhuijsen 2025). At the low resolutions required to have time and resources to evolve the mean field, these simulations have low magnetic Reynolds numbers, which inhibits the SSD and weakens the turbulent constituent (Gressel 2008; Gent 2012). Full galaxy simulations have even lower Reynolds numbers, especially in the low-density, high sound speed regions where dynamo action is most important (Gent et al. 2023). These typically yield merely a turbulent constituent due to insufficient integration time for the mean-field dynamo to grow (Rieder & Teyssier 2016, 2017a,b; Tevlin et al. 2025).

Gent et al. (2021) and Gent et al. (2023) find that the magnetic energy at saturation of the SSD appears to approach an asymptote for magnetic Prandtl numbers $Pm > 10$, though the magnetic Reynolds number is the determining parameter for the strength of the field. How-

Table 1. Models

Model	δx [pc]	Pm	ν_6, χ_6, η_6 [kpc ⁵ km s ⁻¹]	R_{\min} [pc]
N128	2	[1, ∞]	3 (-14)	7.0
N256	1	[1, ∞]	1 (-15)	5.0
N512	1/2	[1, ∞]	4 (-17)	4.5
P512	1/2	[1, 20]	4 (-17)	4.5
P1024	1/4	[1, 100]	2 (-18)	3.8
P2048	1/8	[10,500]	8 (-20)	3.4
P4096	1/16	[100,1000]	4 (-21)	3.2

NOTE—Models to benchmark dependence of η_{crit} on resolution are indicated by N and for testing sensitivity to Pm by P, with the number of grid points on a side given. Viscosity $\nu = 10^{-3}$ kpc km s⁻¹ with the range of $Pm = \nu/\eta$ given in brackets. Sixth order hyperdiffusion coefficients are $\nu_6 = \chi_6 = \eta_6$. R_{\min} is the minimum radial scale R_{SN} of the SN energy injection profile. Parenthesized values give powers of ten.

ever, the grid resolution of those simulations was restricted to $\delta x \in [0.5, 4]$ pc. We, therefore, extend the resolution study to the range $\delta x \in [0.0625, 0.5]$ pc. With any numerical model there is a contribution to the diffusivity from the numerical scheme, which affects the effective Reynolds numbers and is difficult to disentangle from the explicit diffusive parameters in the model. Kriel et al. (2022, 2025) examine a method independent of explicit diffusion to determine the effective diffusivity applying from all sources to a numerical simulation. Here, however, we simply identify the explicit Lagrangian magnetic diffusivity η_{crit} above which the solution varies from that with purely numerical diffusion.

2. MODEL DESIGN

Our model domain is a periodic cubic domain of size $h = 256$ pc on each side containing monatomic gas with mean number density 1 cm^{-3} . SNe explode intermittently at a

¹ <https://www.lumi.csc.fi/public/>

Poisson rate $\dot{\sigma} = 0.75\dot{\sigma}_{\text{Sn}}$ at uniform random locations, where the solar neighbourhood rate $\dot{\sigma}_{\text{Sn}} \simeq 17 \text{ kpc}^{-2} \text{ Myr}^{-1}$ (van den Bergh & Tamman 1991; Mannucci et al. 2005). The volume SN rate is determined using a galactic thickness, which we choose to be the side h of our periodic box. The periodic domain excludes pressure release by galactic winds or fountains, so we choose an SN rate lower than the solar neighbourhood value to avoid thermal runaway (Kim & Ostriker 2015) and maintain a multiphase ISM for the duration of the simulations.

Our models are summarised in Table 1. Those denoted by N apply the kinematic phase of the SSD for benchmarking the magnetic diffusivity η_{crit} that can be resolved at each resolution (Sect. 3). Those denoted by P evolve the SSD for $\eta > \eta_{\text{crit}}$ until saturation of the dynamo is established (Sect. 4). As a common initial condition for the set of P models, a snapshot from Model N512 during its kinematic phase is used. For models with higher resolution, it is remeshed employing cubic interpolation.

To run our models, we use the PENCIL CODE (Pencil Code Collaboration et al. 2021) coupled with the ASTAROTH library (Pekkilä 2019; Pekkilä et al. 2022). This allows us to use GPUs for speedup by as much as a factor of 20 for this problem. We solve the compressible, non-ideal, non-adiabatic system of magnetohydrodynamic equations

$$\frac{D\rho}{Dt} = -\rho \nabla \cdot \mathbf{u} + \nabla \cdot \zeta_D \nabla \rho, \quad (1)$$

$$\begin{aligned} \rho \frac{D\mathbf{u}}{Dt} = & \mu_0^{-1} \nabla \times \mathbf{B} \times \mathbf{B} - \rho c_s^2 \nabla (s/c_p + \ln \rho) \\ & + \nabla \cdot (2\rho\nu \mathbf{W}) + \rho \nabla (\zeta_\nu \nabla \cdot \mathbf{u}) \\ & + \nabla \cdot (2\rho\nu_6 \mathbf{W}^{(5)}) - \mathbf{u} \nabla \cdot (\zeta_D \nabla \rho), \end{aligned} \quad (2)$$

$$\frac{\partial \mathbf{A}}{\partial t} = \mathbf{u} \times \mathbf{B} + \eta \nabla^2 \mathbf{A} + \eta_6 \tilde{\nabla}^6 \mathbf{A}, \quad (3)$$

$$\begin{aligned} \rho T \frac{Ds}{Dt} = & E_{\text{th}} \dot{\sigma} h^{-1} + \rho \Gamma - \rho^2 \Lambda + \eta \mu_0^{-1} |\nabla \times \mathbf{B}|^2 \\ & + 2\rho\nu |\mathbf{W}|^2 + \rho \zeta_\nu (\nabla \cdot \mathbf{u})^2 \\ & + \nabla \cdot (\zeta_\chi \rho T \nabla s) + \rho T \chi_6 \tilde{\nabla}^6 s \\ & - c_v \gamma T (\zeta_D \nabla^2 \rho + \nabla \zeta_D \cdot \nabla \rho), \end{aligned} \quad (4)$$

where ρ denotes the density of the gas, s its specific entropy, T its temperature, and \mathbf{u} its velocity, with c_s the adiabatic sound speed, t the time; \mathbf{A} is the magnetic vector potential, with magnetic field $\mathbf{B} = \nabla \times \mathbf{A}$. The constant μ_0 denotes the vacuum magnetic permeability and c_p and c_v the gas specific heat capacity at constant pressure and constant volume, respectively. The advective derivative

$$\frac{D}{Dt} = \frac{\partial}{\partial t} + \mathbf{u} \cdot \nabla, \quad (5)$$

the traceless rate of strain tensor \mathbf{W} has components

$$\mathbf{W}_{ij} = \frac{1}{2} \left(\frac{\partial u_i}{\partial x_j} + \frac{\partial u_j}{\partial x_i} - \frac{2}{3} \delta_{ij} \nabla \cdot \mathbf{u} \right), \quad (6)$$

and $|\mathbf{W}|^2 = \mathbf{W}_{ij}^2$ is its contraction.²

To manage numerical instabilities near the Nyquist frequency, we apply a sixth order hyperdiffusivity in Eq. (2), proportional to the divergence of $\rho \mathbf{W}^{(5)}$, where

$$\mathbf{W}_{ij}^{(5)} = \tilde{\nabla}^4 \mathbf{W}_{ij}, \quad (7)$$

and in Eqs. (3) and (4) proportional to $\tilde{\nabla}^6 \mathbf{A}$ and $\tilde{\nabla}^6 s$, respectively with³

$$\tilde{\nabla}^4 = \frac{\partial^2}{\partial x_i^2} \frac{\partial^2}{\partial x_i^2}, \quad \tilde{\nabla}^6 = \frac{\partial^3}{\partial x_i^3} \frac{\partial^3}{\partial x_i^3}. \quad (8)$$

The corresponding coefficients $\nu_6 = \eta_6 = \chi_6$ are listed in Table 1. Models at each resolution were tested to find the minimum of ν_6 , for which

² We adopt Einstein's summation convention throughout.

³ Distinct from the biharmonic operator

$\nabla^4 = (\partial^2 / \partial x_i^2)^2$, etc.

the corresponding grid Reynolds number at the Nyquist frequency

$$\text{Re}^{(6)} = \frac{u_{\text{rms}}}{\nu_6 k_{\text{Ny}}^5}, \quad (9)$$

typically peaking shortly after each explosion, would remain below 10 (see Haugen & Brandenburg 2004, which gives more detail on the use of hyperdiffusivity).

To resolve shock discontinuities, artificial diffusion with coefficients

$$\zeta_D, \quad \zeta_\nu, \quad \zeta_\chi = \begin{cases} 0.3 |\nabla \cdot \mathbf{u}|^{7/4} \text{ kpc km s}^{-1}, & \nabla \cdot \mathbf{u} < 0 \\ 0.015 |\nabla \cdot \mathbf{u}|^{7/4} \text{ kpc km s}^{-1}, & \nabla \cdot \mathbf{u} > 0 \end{cases}$$

is applied in Eqs. (1), (2), and (4), respectively. The terms with ζ_D and ζ_χ are almost quadratic in $\nabla \cdot \mathbf{u}$, while the one with ζ_ν is almost cubic. Commonly, such a scheme has been applied only to convergent flows and with the exponent 1 instead of 7/4 (e.g., Gent et al. 2020, with prefactor 1 instead of 0.3). We find it necessary to apply it also, albeit more weakly, to divergent flows to suppress numerical instability there, while the higher exponent better confines the diffusion locally to the shocks.

Expressions containing ζ_D are also included in Eqs. (2) and (4) to correct for momentum and energy conservation. A missing factor in our earlier work of $\gamma = c_p/c_v$ has been included in Eq. (4). Srivastava et al. (2025) found that this correction term prefactor in Eq. (4) significantly impacted the thickness of their modelled solar atmosphere, but it has limited effect in the unstratified turbulent ISM modelled here.

The system is driven and regulated by sources and sinks of heat in Eq. (4). SNe are applied with $E_{\text{th}} = 10^{51}$ erg injected in spheres with a Gaussian radial thermal energy profile of scale $R_{\text{SN}} \geq R_{\text{min}} \in [3.1875, 7]$ pc (as per δx , see Table 1), always chosen to be large enough to contain at least $100 M_\odot$ of ambient gas within R_{SN} . Neither mass nor momentum are included

in the SN injection. Cooling following Sánchez-Salcedo et al. (2002) and Gressel et al. (2008) is implemented (see Gent et al. 2013, Table 1) but with $\Lambda = 0$ for $T < 90$ K, which produces thermally unstable ranges at high and low temperatures as expected for the ISM and uniform far ultraviolet heating Γ is included (Gent et al. 2013).

The ideal gas equation of state closes the system, assuming an adiabatic index $\gamma = c_p/c_v = 5/3$. Treating the ISM as a monatomic, fully ionized plasma we apply a mean molecular weight of 0.531. An important revision to our prior implementations is to replace third-order time integration, constrained primarily by Courant conditions, with a fourth-order accuracy-constrained adaptive time stepping scheme following Kennedy et al. (2000).

3. RESOLUTION OF MAGNETIC DIFFUSIVITY

We choose a viscosity $\nu = 10^{-3}$ kpc km s⁻¹ because we have demonstrated that this value exceeds numerical viscosity at any resolution used in this study (Gent et al. 2021, 2023). By this, we mean that we can distinguish a difference in the energy spectrum from the solution without physical viscosity.

To identify asymptotic behavior of the SSD saturation level with respect to the magnetic Reynolds number $\text{Rm} = l_f u_{\text{rms}}/\eta$ or Prandtl number $\text{Pm} = \nu/\eta$, we need to choose explicit magnetic diffusivities η in our simulations that exceed the numerical diffusivity. Hence, we test what values of η distinguish the solution from that with only hyperdiffusion and shock diffusion in runs during the kinematic phase of the SSD, labelled with N in Table 1. The magnetic energy spectra from these runs, compensated by the Kazantsev $k^{3/2}$ scaling, are plotted in Figure 1. The insets zoom in near the start of the dissipation range, to allow identification of the critical diffusivity η_{crit} above which the deviations from the solutions for $\eta = 0$ become sig-

Table 2. Critical magnetic diffusivity

Model	δx [pc]	η_{crit} [kpc km s $^{-1}$]
N128	2	1 (-4)
N256	1	5 (-5)
N512	1/2	2 (-5)

NOTE—Minimum magnetic diffusivity η_{crit} required to modify solution at each resolution. Parenthesized values give powers of ten.

nificant. These are listed in Table 2 and indicate that $\eta_{\text{crit}} \approx 5 \times 10^{-5} (\delta x / 1 \text{ pc}) \text{ kpc km s}^{-1}$.

4. RESULTS

4.1. Spectral scaling

Magnetic energy spectra for various Pm are displayed in Figure 2 for both N and P model sets. To ease comparison between results during varying stages of the kinematic phase up to and including saturation, each spectrum is normalized by its magnetic energy at the forcing scale, $e_B(k_f)$, where $l_f = 2\pi k_f^{-1} \simeq 50 \text{ pc}$ is the typical forcing scale of the SN remnants as determined by the correlation length of the turbulent velocity near the galactic midplane (Hollins et al. 2017).

In Figure 2(a) with $\text{Pm} = 1$, the spectra for the models of set N in the kinematic phase align with the Kazantsev $k^{3/2}$ scaling for $k < k_f$ (Kazantsev 1968) while the peak energy extends to higher k with increasing resolution. The Kazantsev scaling is also present for the Models P512 and P1024, but relative to Model N512, the energy peak is pushed to lower k , reflecting the apparent saturation of the SSD. This is more clearly evident in Figure 2(d) for $\text{Pm} = 10$ when comparing the spectra for Model P512 with N512 (green, dash-dotted, thick and thin, respectively). Model P512 has reached saturation and its energy peak is at significantly lower $k \simeq 700 \text{ kpc}^{-1}$ than for Model N512 at $k \simeq 1300 \text{ kpc}^{-1}$. Model P1024 is also approaching saturation with peak energy at even lower k

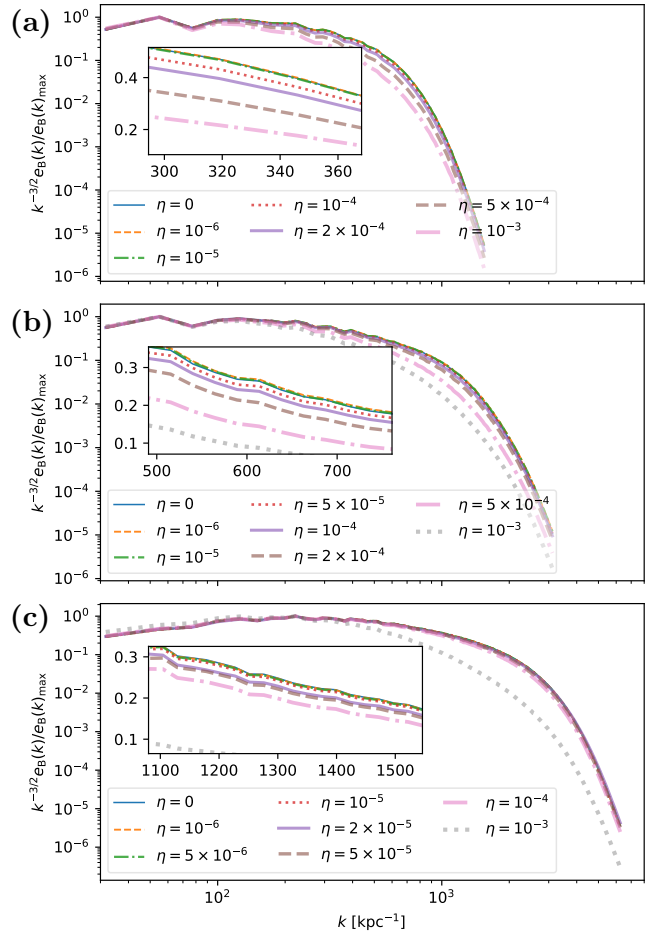


Figure 1. Magnetic energy spectra $e_B(k)$ compensated by the Kazantsev scaling $k^{3/2}$ and normalized by their compensated maximum for (a) Models N128, (b) N256 and (c) N512 using different values of the magnetic diffusivity η in kpc km s^{-1} as listed in the legends. Insets zoom in near the start of the inertial range to highlight deviations from the curve for $\eta = 0$.

than in Model N512, while Model P2048 is still kinematic with its peak located at even higher k . In summary, the peak energy in saturated fields converges at wavenumbers far below the Nyquist frequency, and Kazantsev scaling holds at lower wavenumbers.

4.2. Saturation

We study the saturation of models with varying Pm , Rm , and numerical resolution, always

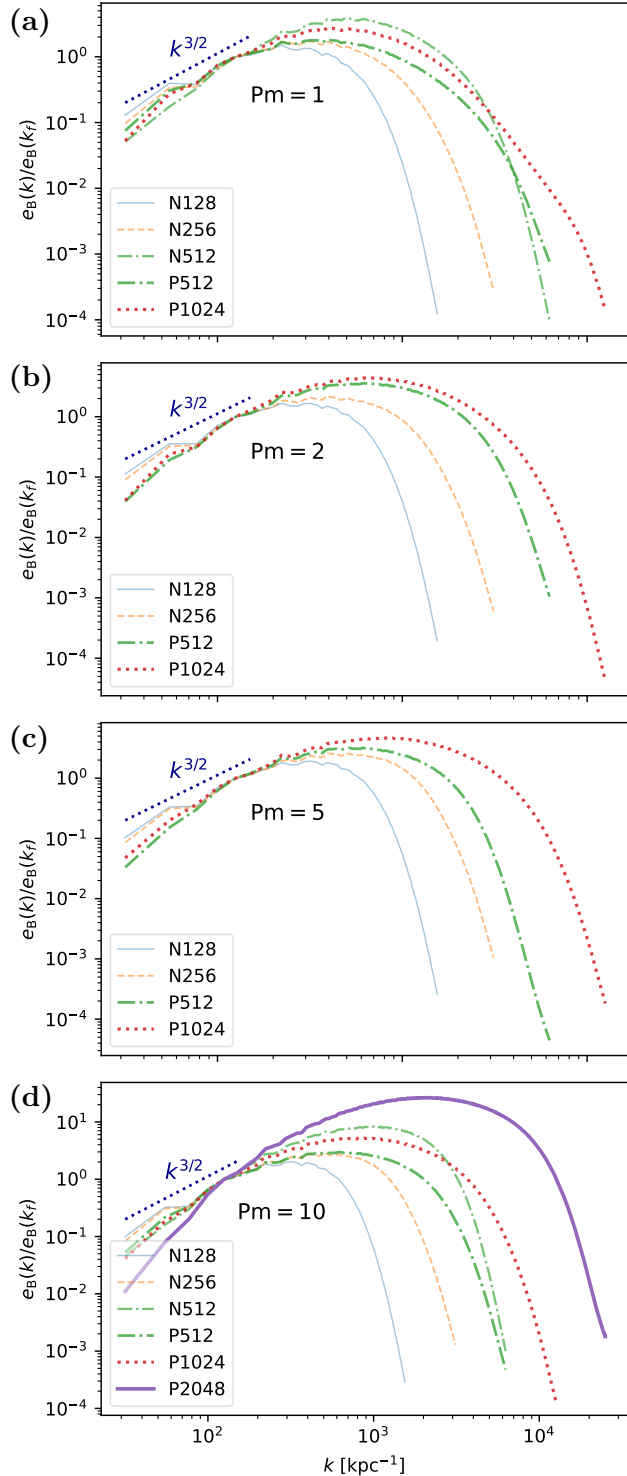


Figure 2. Magnetic energy spectra $e_B(k)$ normalized by $e_B(k_f)$ at a typical SN forcing wavenumber $k_f = 125 \text{ kpc}^{-1}$ at a given Pm for models listed in the legends. The $k^{3/2}$ Kazantsev scaling is indicated upper left (dotted dark blue).

ensuring $\eta > \eta_{\text{crit}}$, so the physical magnetic diffusivity determines the solution.

Figure 3 shows the evolution of the magnetic energy density e_B normalized by the time-averaged kinetic energy density \bar{e}_K for each simulation. Although the only parameter varying at fixed resolution is η , the models can diverge over time as the system is inherently chaotic and the time step differs in each realisation. We therefore mark SN explosions, which can be followed by sudden surges of magnetic energy growth.

Note that growth is substantially faster at higher resolution (Gent et al. 2021), and the time axis covers a correspondingly shorter period of time in each panel. This indicates that the properties of the turbulence are not completely determined by the explicit values of ν and η but also by the higher numerical diffusion at lower resolution.

We measure the strength of the magnetic energy after the SSD has saturated, e_s , relative to \bar{e}_K during the final 2.5% of run time for each simulation, and list these in the legends of Figure 3 and in Table 3. Due to our finite numerical resources, the higher resolution models in Figure 3(c) and (d) are not yet saturated and e_s is a lower limit to the saturation level in these models. Some of the models in Figure 3(a) and (b) also do not appear to have yet fully saturated, so it would be preferable to extend those runs as well. For resolution 2048^3 in Figure 3(c), $e_s = 0.02$ for $Pm = 10$ is consistent with levels obtained at the lower resolution. At higher Rm , e_s remains below those of matching Rm runs at lower resolution. The solutions are close in Figure 3 at $Pm = 20$ for Models P512 and P1024 and the spectra are converging for these two Models at $Pm = 10$ in Figure 2(d). We find that the saturation level of the magnetic field approaches a plateau at around 5% of equipartition with the kinetic energy independent of resolution as Pm increases above 10.

Table 3. SSD saturation energy

η [kpc km s ⁻¹]	Pm	Rm [10 ³]				e_s [$\overline{e_K}$]			
		at resolution [pc]				at resolution [pc]			
		1/2	1/4	1/8	1/16	1/2	1/4	1/8	1/16
1 (-3)	1	2.8	3.0			1 (-7)*	4 (-7)*		
5 (-4)	2	5.8	6.3			2 (-3)	2 (-3)*		
2 (-4)	5	9.1	20			1 (-3)	2 (-3)		
1 (-4)	10	26	29	53		4 (-2)	2 (-2)	5 (-5)	
5 (-5)	20	47	54			4 (-2)*	2 (-2)		
2 (-5)	50			263				7 (-3)	
1 (-5)	100		297	555	644		4 (-2)*	6 (-3)	3 (-7)
5 (-6)	200			1165	921			1 (-2)	4 (-7)
1 (-6)	1000				4475				9 (-4)

NOTE— Dependence of SSD saturation energy on η , Pm, and resolution. u_{rms} rises from 50 to 130 km s⁻¹ between $\delta x = 1/2$ pc and 1/16 pc and varies as much as 25% for a given δx so Rm is not fixed for a given Pm. Mean magnetic energy density e_s is averaged over the final 2.5% of each run normalized by the time-averaged turbulent kinetic energy density $\overline{e_K}$. Asterisks indicate runs where the field appears saturated.

The current results at resolutions of 512³ and 1024³ are strong evidence that the magnetic energy at saturation of the SSD is asymptotic at Pm or Rm levels far below those of the real ISM and within reach of numerical simulations. This is consistent with the results of Schekochihin et al. (2004) and Schober et al. (2015) for isothermal, compressible plasmas with artificial forcing, who find an asymptotic value of the saturation energy below 10% of equipartition with the kinetic energy at Pm $\lesssim 100$.

5. SUMMARY AND CONCLUSIONS

Models with increasing magnetic Prandtl number Pm show that the magnetic energy density amplified by the SSD in the ISM saturates at about 5% of the turbulent kinetic energy density significantly below the turbulent magnetic field energy density estimated from observations. This occurs at relatively low Prandtl numbers Pm of order 10–100 while estimates of the actual Pm for the ISM are in the range 10¹⁰–10¹⁴ (Brandenburg & Subramanian 2005).

In this study we have not considered the variation of the fluid Reynolds number Re, because in previous experiments Rm rather than Pm has been found to be the determining parameter for the SSD properties (Oishi & Mac Low 2011; Gent et al. 2021, 2023). However, these results were at much lower resolution, so the effect of Re should still be tested at high resolution. It is possible that we have a false convergence in the properties of the SSD (Fryxell et al. 1991), and that at even higher Rm, new behaviour emerges. In Gent et al. (2021), a false convergence of magnetic decay for $\delta x \geq 2$ pc at $\eta = 10^{-3}$ kpc km s⁻¹ and $\nu = 0$ is contradicted at $\delta x \leq 1$ pc, for which SSD is present. However, this can be explained by the numerical diffusion dominating over the physical diffusion, whereas here we have ensured that $\eta > \eta_{\text{crit}}$, so any qualitative change in the behaviour of the SSD would imply that new or additional physics are acting at the smaller scales.

In these experiments, we have yet to see convergence of the growth rate of the SSD, with faster growth at higher Rm and also at higher

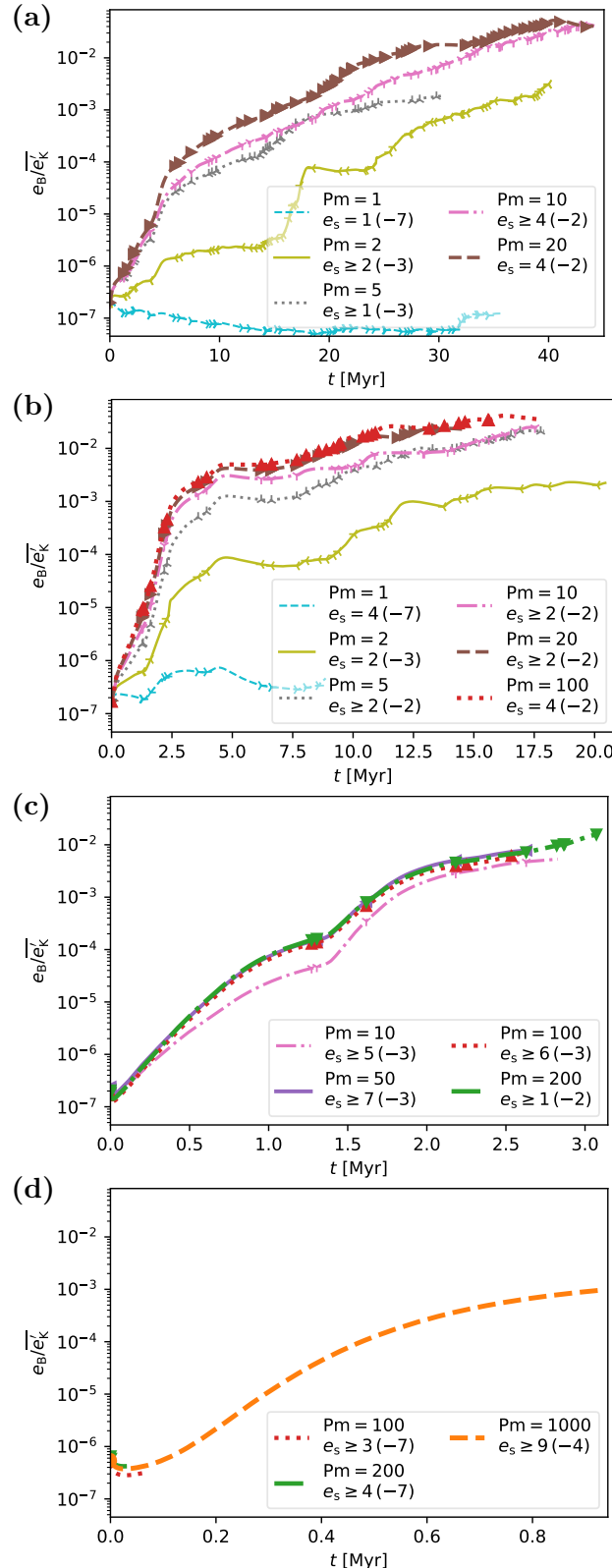


Figure 3. Magnetic energy e_B normalised by time-averaged turbulent kinetic energy \bar{e}_K for grid (a) 512^3 (b), 1024^3 (c), 2048^3 and (d) 4096^3 . See the legends for Pm and e_s from an average over the latest 2.5% of simulation time. Markers are shown at the time of SN explosions. Note that the time scales are dramatically smaller at higher resolution.

resolution. From our highest resolution runs, we can verify that in the ISM we would expect to see an established turbulent magnetic field at 5% of equipartition with the turbulent kinetic energy within less than 1–2 Myr. This is on timescales that are almost negligible for cosmological, galaxy cluster, or full galaxy simulations in which it is unfeasible to produce by dynamo such strong magnetic fields on timescales that can be reached on current computational resources. It would therefore be worth considering including these turbulent fields as an input to such simulations at the outset. For such models and also for LSD models, the SSD would be too slow, and the benefit of our results would be to model the characteristics and strength of the turbulent magnetic field either by a subgrid-scale model or another method to ensure its effect is present.

Our magnetic energy spectra suggest that an addition to the simulated magnetic field, which exhibits the Kazantsev $k^{3/2}$ scaling at all k could be included in an LSD or galactic simulation. Gent et al. (2024) observe that the spectrum during the kinematic dynamo stage has the same scaling at low k , but its peak shifting to lower k due to tangling. In this phase, the largest scales of the LSD grow most rapidly eventually superseding the Kazantsev scaling. So, the energy peak beyond which this scaling disappears does appear to move to lower k as the SSD driven field saturates, but to find whether or where this becomes asymptotic with increasing Rm would require continuation of the models in this work, particularly at the highest resolution, beyond saturation of the SSD. In most practical models of LSD or galaxy evolution, it is likely that this peak in any case applies below their grid resolution. From this perspective the structure of the turbulent field does not appear to depend on whether it is derived by SSD or tangling. How to add an artificial turbulent field and whether to apply it

proportional to the energy density of the total or the large-scale magnetic field, the turbulent kinetic energy density or other parameters requires further analysis.

Facilities: The authors wish to acknowledge CSC – IT Center for Science, Finland, for computational resources. We acknowledge the EuroHPC Joint Undertaking for awarding this project access to the EuroHPC supercomputer LUMI, hosted by CSC (Finland) and the LUMI consortium through a EuroHPC Extreme Scale Access call.

Software: PENCIL CODE (Brandenburg & Dobler 2002; Pencil Code Collaboration et al. 2021) ASTAROTH

(Pekkilä 2019; Pekkilä et al. 2022)

1 We thank C. F. Gammie, C. Federrath, and J.
 2 Beattie for useful discussion of resolution diag-
 3 nostics and S. Srivastava & P Chatterjee for dis-
 4 cussion regarding the energy conservation term
 5 in Eq. (4). F.A.G. benefited from in-depth dis-
 6 cussions at “Towards a Comprehensive Model
 7 of the Galactic Magnetic Field” at Nordita 2023
 8 supported by NordForsk and acknowledges sup-
 9 port of the Swedish Research Council (Veten-
 10 skapsrådet) grant no. 2022-03767. M.J.K.-L.,
 11 M.R. and T.P. acknowledge support from the
 12 ERC under the EU’s Horizon 2020 research and
 13 innovation programme (Project UniSDyn, grant
 14 818665). M-M.M.L. was partly supported by
 15 US NSF grant AST23-07950, and thanks the
 16 Inst. für Theoretische Astrophysik der Uni. Hei-
 17 delberg for hospitality. His research was also
 18 supported in part by grant NSF PHY-2309135
 19 to the Kavli Institute for Theoretical Physics
 20 (KITP).

REFERENCES

Beck, R. 2015, A&A Rv, 24, 4,
 doi: [10.1007/s00159-015-0084-4](https://doi.org/10.1007/s00159-015-0084-4)

Beck, R., & Berkhuijsen, E. M. 2025, A&A, 700,
 A198, doi: [10.1051/0004-6361/202555048](https://doi.org/10.1051/0004-6361/202555048)

Brandenburg, A., & Dobler, W. 2002, Computer
 Physics Communications, 147, 471

Brandenburg, A., & Subramanian, K. 2005, PhR,
 417, 1, doi: [10.1016/j.physrep.2005.06.005](https://doi.org/10.1016/j.physrep.2005.06.005)

Fryxell, B., Mueller, E., & Arnett, D. 1991, ApJ,
 367, 619, doi: [10.1086/169657](https://doi.org/10.1086/169657)

Gent, F. A. 2012, PhD thesis, Newcastle
 University School of Mathematics and Statistics

Gent, F. A., Mac Low, M.-M., Käpylä, M. J.,
 Sarson, G. R., & Hollins, J. F. 2020,
 Geophysical and Astrophysical Fluid Dynamics,
 114, 77, doi: [10.1080/03091929.2019.1634705](https://doi.org/10.1080/03091929.2019.1634705)

Gent, F. A., Mac Low, M.-M., Käpylä, M. J., &
 Singh, N. K. 2021, ApJL, 910, L15,
 doi: [10.3847/2041-8213/abed59](https://doi.org/10.3847/2041-8213/abed59)

Gent, F. A., Mac Low, M.-M., & Korpi-Lagg,
 M. J. 2024, ApJ, 961, 7,
 doi: [10.3847/1538-4357/ad0da0](https://doi.org/10.3847/1538-4357/ad0da0)

Gent, F. A., Mac Low, M.-M., Korpi-Lagg, M. J.,
 & Singh, N. K. 2023, ApJ, 943, 176,
 doi: [10.3847/1538-4357/acac20](https://doi.org/10.3847/1538-4357/acac20)

Gent, F. A., Shukurov, A., Fletcher, A., Sarson,
 G. R., & Mantere, M. J. 2013, MNRAS, 432,
 1396, doi: [10.1093/mnras/stt560](https://doi.org/10.1093/mnras/stt560)

Gressel, O. 2008, PhD thesis, Astrophysikalisches
 Institut Potsdam

Gressel, O., Ziegler, U., Elstner, D., & Rüdiger, G.
 2008, Astronomische Nachrichten, 329, 619,
 doi: [10.1002/asna.200811005](https://doi.org/10.1002/asna.200811005)

Haugen, N. E. L., & Brandenburg, A. 2004,
 PhRvE, 70, 036408,
 doi: [10.1103/PhysRevE.70.036408](https://doi.org/10.1103/PhysRevE.70.036408)

Hollins, J. F., Sarson, G. R., Shukurov, A.,
 Fletcher, A., & Gent, F. A. 2017, ApJ, 850, 4,
 doi: [10.3847/1538-4357/aa93e7](https://doi.org/10.3847/1538-4357/aa93e7)

Kazantsev, A. P. 1968, Soviet Journal of Experimental and Theoretical Physics, 26, 1031

Kennedy, C. A., Carpenter, M. H., & Lewis, R. M. 2000, Applied Numerical Mathematics, 35, 177. <https://api.semanticscholar.org/CorpusID:15438200>

Kim, C.-G., & Ostriker, E. C. 2015, ApJ, 802, 99, doi: [10.1088/0004-637X/802/2/99](https://doi.org/10.1088/0004-637X/802/2/99)

Kriel, N., Beattie, J. R., Federrath, C., Krumholz, M. R., & Hew, J. K. J. 2025, MNRAS, 537, 2602, doi: [10.1093/mnras/staf188](https://doi.org/10.1093/mnras/staf188)

Kriel, N., Beattie, J. R., Seta, A., & Federrath, C. 2022, MNRAS, 513, 2457, doi: [10.1093/mnras/stac969](https://doi.org/10.1093/mnras/stac969)

Mannucci, F., Della Valle, M., Panagia, N., et al. 2005, A&A, 433, 807, doi: [10.1051/0004-6361:20041411](https://doi.org/10.1051/0004-6361:20041411)

Oishi, J. S., & Mac Low, M.-M. 2011, ApJ, 740, 18

Pekkilä, J. 2019. <https://aaltodoc.aalto.fi/server/api/core/bitstreams/c73ad7b3-47a2-4c23-b802-7721366fb961/content>

Pekkilä, J., Väisälä, M. S., Käpylä, M. J., Rheinhardt, M., & Lappi, O. 2022, Parallel Computing, 111, 102904

Pencil Code Collaboration, Brandenburg, A., Johansen, A., et al. 2021, The Journal of Open Source Software, 6, 2807, doi: [10.21105/joss.02807](https://doi.org/10.21105/joss.02807)

Rieder, M., & Teyssier, R. 2016, MNRAS, 457, 1722, doi: [10.1093/mnras/stv2985](https://doi.org/10.1093/mnras/stv2985)

—. 2017a, MNRAS, 471, 2674, doi: [10.1093/mnras/stx1670](https://doi.org/10.1093/mnras/stx1670)

—. 2017b, MNRAS, 472, 4368, doi: [10.1093/mnras/stx2276](https://doi.org/10.1093/mnras/stx2276)

Sánchez-Salcedo, F. J., Vázquez-Semadeni, E., & Gazol, A. 2002, ApJ, 577, 768, doi: [10.1086/342223](https://doi.org/10.1086/342223)

Schekochihin, A. A., Cowley, S. C., Taylor, S. F., Maron, J. L., & McWilliams, J. C. 2004, ApJ, 612, 276, doi: [10.1086/422547](https://doi.org/10.1086/422547)

Schober, J., Schleicher, D. R. G., Federrath, C., Bovino, S., & Klessen, R. S. 2015, PhRvE, 92, 023010, doi: [10.1103/PhysRevE.92.023010](https://doi.org/10.1103/PhysRevE.92.023010)

Srivastava, S., Chatterjee, P., Dey, S., & Erdélyi, R. 2025, ApJ, 989, 39, doi: [10.3847/1538-4357/ade9b4](https://doi.org/10.3847/1538-4357/ade9b4)

Tevlin, L., Berlok, T., Pfrommer, C., et al. 2025, A&A, 701, A114, doi: [10.1051/0004-6361/202452823](https://doi.org/10.1051/0004-6361/202452823)

van den Bergh, S., & Tammann, G. A. 1991, ARA&A, 29, 363, doi: [10.1146/annurev.aa.29.090191.002051](https://doi.org/10.1146/annurev.aa.29.090191.002051)